



OPEN

Elastic, electronic and optical properties of new 2D and 3D boron nitrides

Huayue Mei, Yuhan Zhong, Dafang He, Xue Du, Chunmei Li & Nanpu Cheng✉

The current work investigates a novel three-dimensional boron nitride called bulk B_4N_4 and its corresponding two-dimensional monolayer B_4N_4 based on the first-principles of density functional theory. The phonon spectra prove that bulk B_4N_4 and monolayer B_4N_4 are dynamically stable. The molecular dynamics simulations verify that bulk B_4N_4 and monolayer B_4N_4 have excellent thermal stability of withstanding temperature up to 1000 K. The calculated elastic constants state that bulk B_4N_4 and monolayer B_4N_4 are mechanically stable, and bulk B_4N_4 has strong anisotropy. The theoretically obtained electronic structures reveal that bulk B_4N_4 is an indirect band-gap semiconductor with a band gap of 5.4 eV, while monolayer B_4N_4 has a direct band gap of 6.1 eV. The valence band maximum is mainly contributed from B-2p and N-2p orbitals, and the conduction band minimum mainly derives from B-2p orbitals. The electron transitions from occupied N-2p states to empty B-2p states play important roles in the dielectric functions of bulk B_4N_4 and monolayer B_4N_4 . The newly proposed monolayer B_4N_4 is a potential candidate for designing optoelectronic devices such as transparent electrodes due to its high transmissivity.

In recent years, the physicochemical properties of boron nitrides in different crystal structures are widely studied¹. Besides the work on the four common boron nitrides, namely hexagonal boron nitride (h-BN)², rhombohedral boron nitride (r-BN)³, cubic boron nitride (c-BN)⁴ and wurtzite boron nitride (w-BN)⁵, researchers have also devoted themselves to the preparations and properties of BN nanosheets⁶. Low dimensional BN nanomaterials, such as h-BN, are famous for their excellent chemical inertness and thermal stability⁷. L. Li *et al.* studied the effect of thicknesses of h-BN on the electric field screening by electrostatic force microscopy (EFM) and theoretical calculations, and found that h-BN is excellent dielectric substrate to support two-dimensional (2D) nanomaterials such as graphene, and MoS₂⁸. J. Li *et al.* calculated the geometrical evolutions, electronic structures and magnetic features of (111) plane-hydrogenated c-BN nanosheets, and pointed out that they can be applied to novel high-performance optoelectronic, spintronic and electronic nanodevices⁹. S. Lin *et al.* investigated the metal-free Si-doped h-BN nanosheets (Si-BNNS), and stated that they are highly stable and active CO oxidation catalysts¹⁰. Further, the amorphous boron nitride with a band gap of 2.0 eV¹¹, Al-doped boron nitride nanosheets with mono-vacancy defects for adsorbing formaldehyde¹², and hydrogen storage properties of oxygen-doped boron nitride nanosheets were also studied¹³.

New structures distinct from the common boron nitrides mentioned above are also the goals explored constantly by researchers. K. Doll *et al.* reported ten two-dimensional layered and three-dimensional (3D) network boron nitrides through *ab initio* simulated annealing¹⁴. X. Li *et al.* predicted three single-layered boron nitride sheets with sp^2 and sp hybrid chemical bonds, and these single-layered boron nitride sheets have promising applications in nanoscale electronic and optoelectronic devices by tuning their band gaps through changing the sp -bond lengths in the boron nitride sheets¹⁵.

In the current work, we investigated a novel 3D monoclinic boron nitride (bulk B_4N_4) which was ever proposed by K. Doll¹⁴ through the CRYSTAL06 code based on local Gaussian-type orbitals. Bulk B_4N_4 consists of BN monolayers connected by van der Waals force, and there is still lack of researches on its properties. Further, the special monoclinic B_4N_4 structure with neighboring atomic layers bonded by van der Waals force inspired us to build its corresponding one-layered sheet (monolayer B_4N_4). Their structural stabilities were verified by the calculations of phonon spectra, molecular dynamics (MD) simulations and elastic constants. Moreover, the mechanical properties, electronic structures and optical properties of bulk B_4N_4 and monolayer B_4N_4 were calculated to reveal their physical properties in detail, which is beneficial to future experimental studies and potential performances.

School of Materials and Energy, Southwest University, Chongqing, 400715, China. ✉e-mail: cheng_np@swu.edu.cn

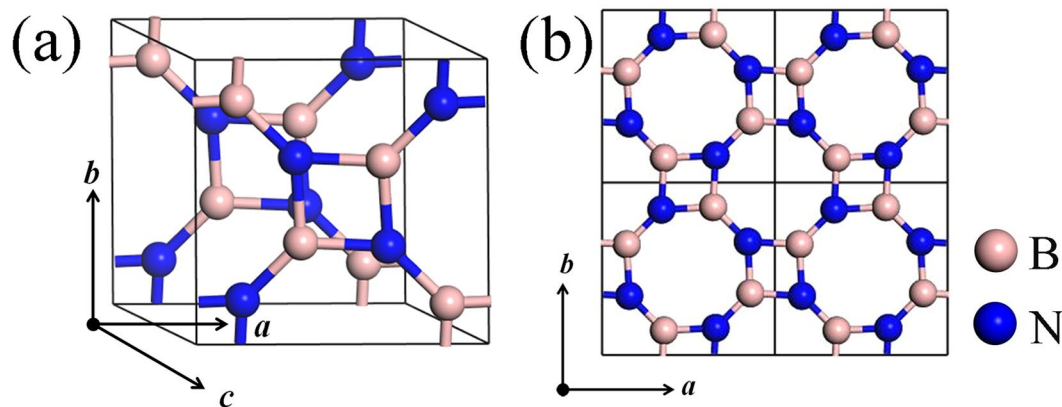


Figure 1. Crystal structures of (a) bulk B_4N_4 and (b) monolayer B_4N_4 ($2 \times 2 \times 1$ super cell).

Theoretical Methods and Models

The current calculations were performed by Cambridge Sequential Total Energy Package (CASTEP) which is a quantum computing program based on density functional theory¹⁶. The generalized gradient approximation (GGA) proposed by Perdew-Burke-Ernzerhof (PBE)¹⁷ was adopted to describe the electronic exchange-correlation term, and the ultrasoft pseudopotential was applied to depict the interaction between valence electrons and ion core during the calculations of geometry optimization, phonon spectra and mechanical properties. We used the hybrid functional PBE0 and the norm conserving pseudopotentials to calculate the electronic structures and optical properties of bulk B_4N_4 and monolayer B_4N_4 , because the GGA-PBE level often underestimates the band gaps of semiconductors due to the discontinuity of exchange correlation energy^{18,19}. The energy cutoffs for the plane wave basis expansion were respectively 280 and 770 eV corresponding to the ultrasoft pseudopotentials and the norm conserving pseudopotentials. The k -points were set to $5 \times 3 \times 3$ and $3 \times 3 \times 1$ Monkhorst-Pack grids for bulk B_4N_4 and monolayer B_4N_4 , respectively. A vacuum space of 20 Å was chosen to avoid the interlayer interaction for monolayer B_4N_4 . The MD simulations in $2 \times 2 \times 1$ supercells of bulk B_4N_4 and monolayer B_4N_4 within the canonical ensemble (NVT) were calculated at room temperature (300 K) and high temperature (1000 K) for 5 ps with a time step of 1 fs. The convergence thresholds of geometry optimization adopting the Broyden-Fletcher-Goldfarb-Shanno (BFGS) method²⁰ satisfied the following conditions: the total energy was less than 5×10^{-6} eV/atom, the ionic force was within 0.01 eV/Å, the stress component was below 0.02 GPa, and the atomic displacement value was less than 5×10^{-4} Å. The valence electrons were B $2s^2 2p^1$ and N $2s^2 2p^3$ during all the calculations.

Results and Discussions

Belonging to the monoclinic system, the unit cell of bulk B_4N_4 with P21/c space group (No.14) includes four B atoms and four N atoms, seeing Fig. 1(a). The optimized lattice parameters of bulk B_4N_4 are $a = 4.9199$ Å, $b = 4.9294$ Å, $c = 3.3738$ Å, $\alpha = 115.11^\circ$ and $\beta = \gamma = 90^\circ$. Interestingly, B_4N_4 crystal consists of BN monolayers connected by van der Waals force along the c -axis. The monolayer B_4N_4 is composed of four- and eight-membered rings. The four-membered rings have bond lengths of 1.48 Å and bond angles of 84.26° and 95.74° . The eight-membered rings consist of two different B-N bonds with bond lengths of 1.48 and 1.40 Å and bond angles of 137.62° and 132.47° , respectively. B atoms occupy the $4e$ sites while N atoms prefer to occupy the $6c$ sites. Due to the weak van der Waals force between two neighboring atomic layers of bulk B_4N_4 along the c -axis, it is easy for them to form monolayers (Fig. 1(b)). The optimized lattice constants of monolayer B_4N_4 are $a = b = 4.9422$ Å and $\gamma = 90^\circ$.

It is well known that phonon dispersion relations can reveal the structural stability of materials. As shown in Fig. 2, there is no imaginary frequency to be found in the phonon spectra of bulk B_4N_4 and monolayer B_4N_4 , indicating that they are dynamically stable. Both the phonon spectra of bulk B_4N_4 and monolayer B_4N_4 have 24 kinds of dispersion relations, including three acoustic branches and 21 optical branches, because there are respectively eight atoms in each unit cell of bulk B_4N_4 and monolayer B_4N_4 . The time-dependent potential energy fluctuations within 5 ps in MD simulations of bulk B_4N_4 and monolayer B_4N_4 plotted in Fig. 3 further verify that they are thermally stable over a wide temperature range. The geometrical structures of bulk B_4N_4 and monolayer B_4N_4 have changed to some extent, and the deformation degree at high temperature is greater than that at room temperature. As a whole, bulk B_4N_4 and monolayer B_4N_4 have very small potential energy fluctuations throughout the MD simulations, suggesting that they can maintain their stable crystal structures at 300 K, even at 1000 K.

Mechanical properties. The unique crystal structures of bulk B_4N_4 and monolayer B_4N_4 would bring interesting mechanical properties under principal and/or shear strains. For the monoclinic B_4N_4 system, there are 13 independent elastic constants, C_{11} , C_{22} , C_{33} , C_{44} , C_{55} , C_{66} , C_{12} , C_{13} , C_{14} , C_{23} , C_{24} , C_{34} and C_{56} (in unit of GPa) in the 6×6 stiffness tensor matrix, and they are written as:

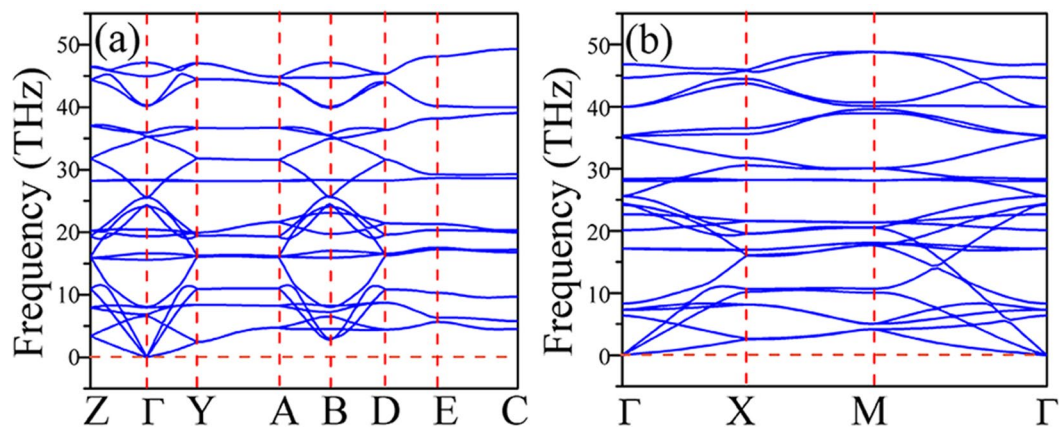


Figure 2. Phonon dispersion relations of (a) bulk B_4N_4 and (b) monolayer B_4N_4 .

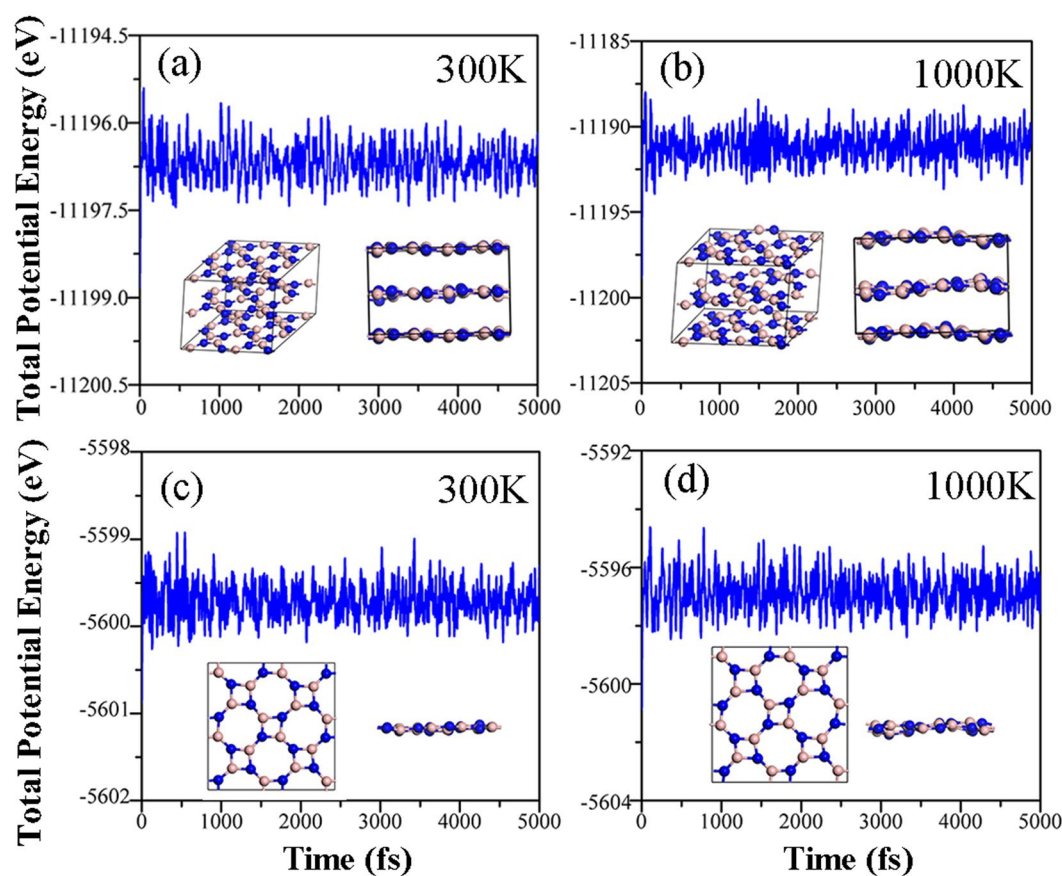


Figure 3. Time-dependent potential energy fluctuations of bulk B_4N_4 and monolayer B_4N_4 at 300 and 1000 K.

$$C_{ij} = \begin{pmatrix} 573.36 & 353.33 & -2.73 & 2.22 & 0 & 0 \\ 353.33 & 568.83 & -2.09 & -2.78 & 0 & 0 \\ -2.73 & -2.09 & 34.52 & -0.57 & 0 & 0 \\ 0 & 0 & 0 & 5.88 & 0 & 0 \\ 2.22 & -2.78 & -0.57 & 0 & 1.51 & 0.96 \\ 0 & 0 & 0 & 0 & 0.96 & 318.86 \end{pmatrix} \quad (1)$$

For the two-dimensional monolayer B_4N_4 , the calculated independent elastic constants, C_{11} , C_{12} , C_{22} and C_{66} (in unit of N/m), in the stiffness tensor matrix are:

	<i>B</i>	<i>G</i>	<i>E_x</i>	<i>E_y</i>	<i>E_z</i>	<i>E</i>	<i>ν</i>
bulk B ₄ N ₄	119.97	63.05	351.19	348.13	34.46	160.96	0.27

Table 1. The calculated bulk modulus (*B*, GPa), shear modulus (*G*, GPa), Young’s modulus (*E*, GPa) and Poisson’s ratio (*ν*) of bulk B₄N₄.

	<i>γ</i>	<i>G</i>	<i>E_x</i>	<i>E_y</i>	<i>E</i>	<i>ν</i>
monolayer B ₄ N ₄	150.24	104.06	114.02	114.02	114.02	0.62

Table 2. The calculated layer modulus (*γ*, N/m), shear modulus (*G*, N/m), Young’s modulus (*E*, N/m) and Poisson’s ratio (*ν*) of monolayer B₄N₄.

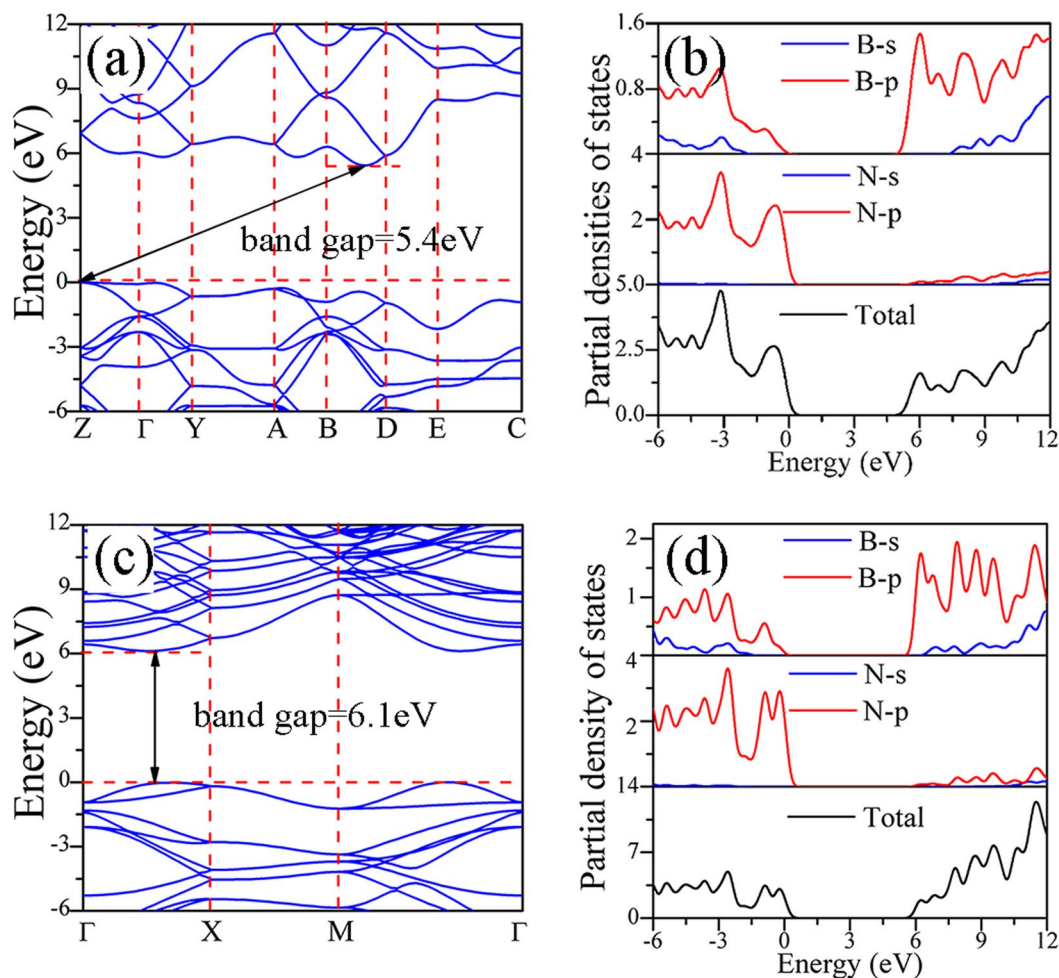


Figure 4. Band structures and partial densities of states of (a,b) bulk B₄N₄ and (c,d) monolayer B₄N₄.

$$C_{ij} = \begin{pmatrix} 185.42 & 115.06 & \dots & 0 \\ 115.06 & 185.42 & \dots & 0 \\ \vdots & \vdots & \ddots & \vdots \\ 0 & 0 & \dots & 104.06 \end{pmatrix} \quad (2)$$

According to the Born-Huang criterion²¹, the mechanical stability of a monoclinic system satisfies:

$$C_{11} > 0, C_{22} > 0, C_{33} > 0, C_{44} > 0, C_{55} > 0, C_{66} > 0,$$

$$(C_{33}C_{55} - C_{35}^2) > 0, (C_{44}C_{66} - C_{46}^2) > 0, (C_{22} + C_{33} - 2C_{23}) > 0,$$

	GGA-PBE	PBE0	Exp.
bulk B ₄ N ₄	3.5	5.4	/
monolayer B ₄ N ₄	4.1	6.1	/
c-BN	4.5	6.5	6.0 ^a , 6.4 ^b
h-BN	4.4	6.2	5.9 ^c , 5.8 ^d

Table 3. Band gaps of bulk B₄N₄, monolayer B₄N₄, c-BN, and h-BN. ^{a,b}Ref. ²⁸, ^cref. ²⁹ and ^dref. ²⁷

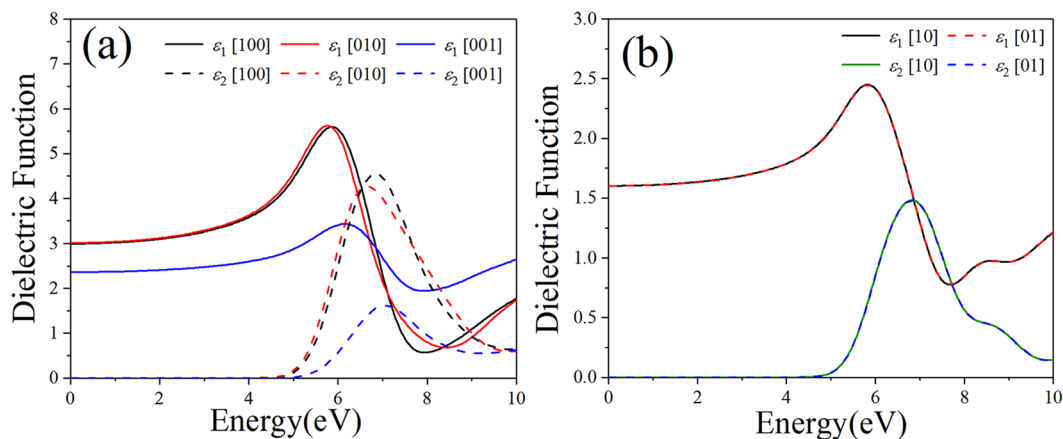


Figure 5. The dielectric functions of (a,c) bulk B₄N₄ and (b,d) monolayer B₄N₄.

$$[C_{11} + C_{22} + C_{33} + 2(C_{12} + C_{13} + C_{23})] > 0 \quad (3)$$

For a two-dimensional monolayer, its structural mechanical stability requires²¹:

$$C_{11}C_{22} - C_{12}^2 > 0, \quad C_{66} > 0 \quad (4)$$

It is obvious that the elastic constants of bulk B₄N₄ satisfy the conditions mentioned in Eq. (3), suggesting that bulk B₄N₄ is mechanically stable under elastic strain perturbations. Due to the weak van der Waals force parallel to the *z* direction, *C*₃₃ is much smaller than *C*₁₁ and *C*₂₂, indicating that the *z* direction of bulk B₄N₄ is easier to deform than the *x* and *y* directions. At the same time, *C*₆₆ is much larger than *C*₄₄ and *C*₅₅, meaning that the *xy* plane has higher ability to resist shear deformation than the *xz* and *yz* planes. From *C*_{*ij*} values of monolayer B₄N₄ and Eq. (4), we know that monolayer B₄N₄ is also mechanically stable. Other elastic parameters of bulk B₄N₄ and monolayer B₄N₄, such as the bulk moduli (*B*), shear moduli (*G*), elastic moduli (*E*) and Poisson's ratios (*ν*), calculated by the Voigt-Ruess-Hill method^{22–24} are respectively shown in Tables 1 and 2. Particularly, similar to the bulk modulus (*B*), the layer modulus (*γ*) in Table 2 represents the ability of two-dimensional materials to resist plane strains.

From Table 1, we can see that the Young's moduli of bulk B₄N₄ vary greatly along different directions, indicating that bulk B₄N₄ has strong anisotropy. *E*_{*z*} = 34.46 GPa, which is much smaller than *E*_{*x*} = 351.19 GPa and *E*_{*y*} = 348.13 GPa, showing the low strength of bulk B₄N₄ along the *z* direction because of the weak van der Waals force. In Table 1, the Young's moduli in the *x* and *y* directions are very close, and the *xy* plane has high strength. We also calculated the universal anisotropy index (*A*^U) expressed by the following formula²⁵:

$$A^U = 5 \frac{G_V}{G_R} + \frac{B_V}{B_R} - 6 \geq 0 \quad (5)$$

The calculated *A*^U = 107.37 indicates that bulk B₄N₄ has strong anisotropy, which is the manifestation that the components of Young's moduli vary greatly in different directions. The Young's moduli of monolayer B₄N₄ in the *x* and *y* directions are equal due to the square symmetric structures. Besides, monolayer B₄N₄ has a special large Poisson's ratio of 0.62, and it should be attributed to the loose arrangements of atoms allowing greater contractions during deformation²⁶.

Electronic structures. Figure 4 shows the band structures and partial densities of states of bulk B₄N₄ and monolayer B₄N₄ in the first Brillouin zone. The Fermi level is set to zero. Bulk B₄N₄ has an indirect band gap of 5.4 eV, while monolayer B₄N₄ has a direct band gap of 6.1 eV. In Table 3, the band gaps of c-BN and h-BN calculated by the hybrid functional PBE0 are in good agreement with the experimental values^{27–29}, so we can deduce that PBE0 is suitable to estimate the band gaps of bulk B₄N₄ and monolayer B₄N₄. The obtained band gap of monolayer B₄N₄ is close to those of c-BN and h-BN, and the band gap of bulk B₄N₄ is slightly smaller than those

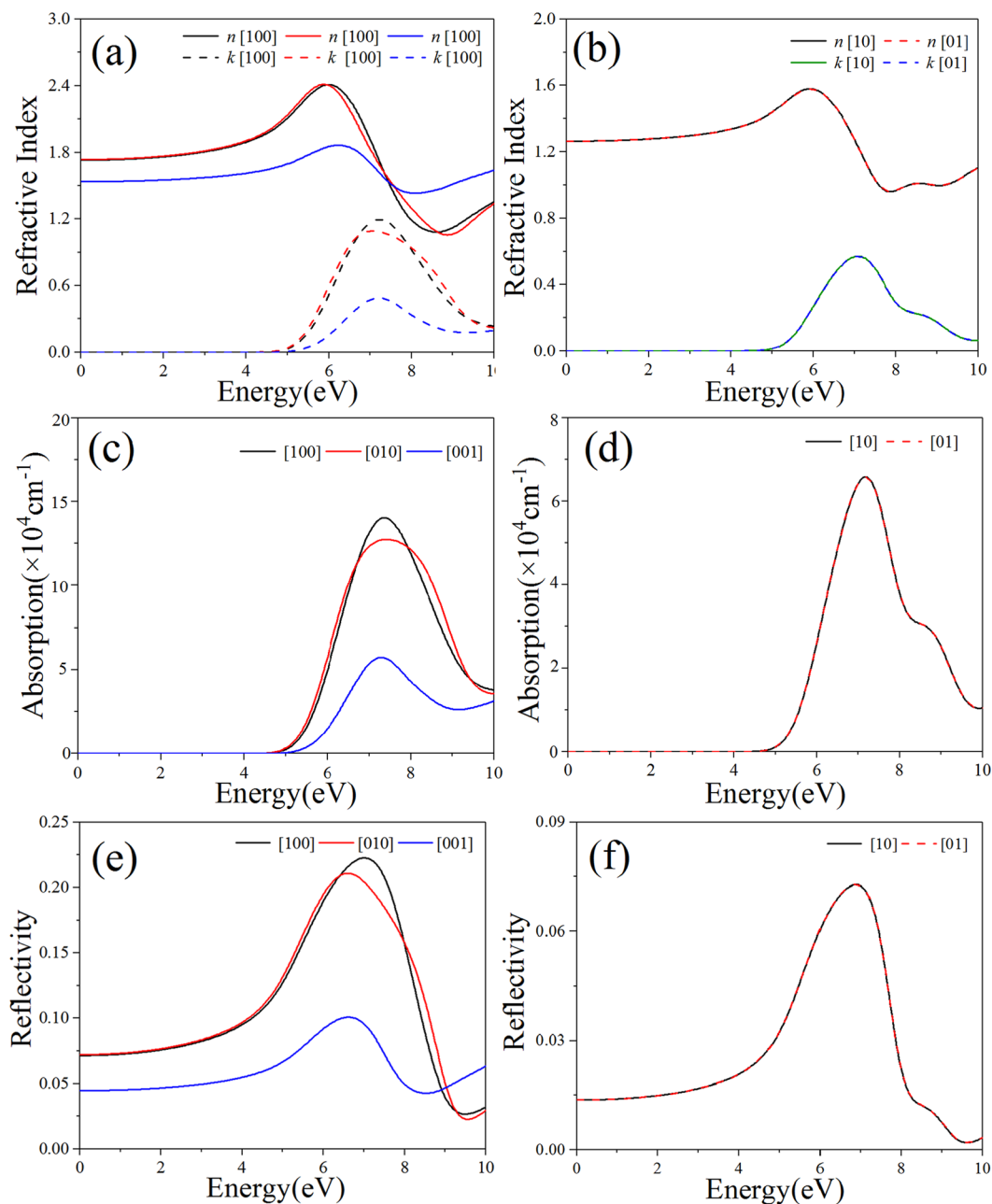


Figure 6. The refractive indexes, absorption coefficients and reflectivities of (a,c,e) bulk B_4N_4 and (b,d,f) monolayer B_4N_4 .

of c-BN, h-BN and B_4N_4 nanosheet. From the partial densities of states of bulk B_4N_4 and monolayer B_4N_4 , the valence band maximum (VBM) is mainly contributed from B-2*p* and N-2*p* hybrid orbitals, and the conduction band minimum (CBM) mainly derives from B-2*p* orbitals.

Optical properties. The optical properties of some a medium can be described by the complex dielectric function: $\varepsilon(\omega) = \varepsilon_1(\omega) + i\varepsilon_2(\omega)$ ^{30,31}. The real part $\varepsilon_1(\omega)$ characterizes the polarization degree of medium under an external electric field. The imaginary part $\varepsilon_2(\omega)$ corresponding to the interband electron transitions from occupied states to unoccupied states can be obtained by calculating the momentum matrix elements of the wave function, and then $\varepsilon_1(\omega)$ can be obtained from the Kramers–Kronig correlation^{32,33}. Because bulk B_4N_4 belongs to the monoclinic system, it is necessary to consider the optical anisotropy of bulk B_4N_4 and its corresponding monolayer B_4N_4 . Figure 5 shows the direction-dependent dielectric functions of bulk B_4N_4 and monolayer B_4N_4 in the energy range of 0–10 eV. For bulk B_4N_4 , see Fig. 5(a), the photon energy-dependent intensities and peak positions of dielectric functions in [100] and [010] directions are slightly different, while those in [001] direction are quietly different, which should be attributed to the influence of van der Waals force in [001] direction, see Fig. 1(a). The calculated static dielectric constants $\varepsilon_1^{[100]}(0)$, $\varepsilon_1^{[010]}(0)$ and $\varepsilon_1^{[001]}(0)$ of bulk B_4N_4 are respectively 2.99, 3.01 and

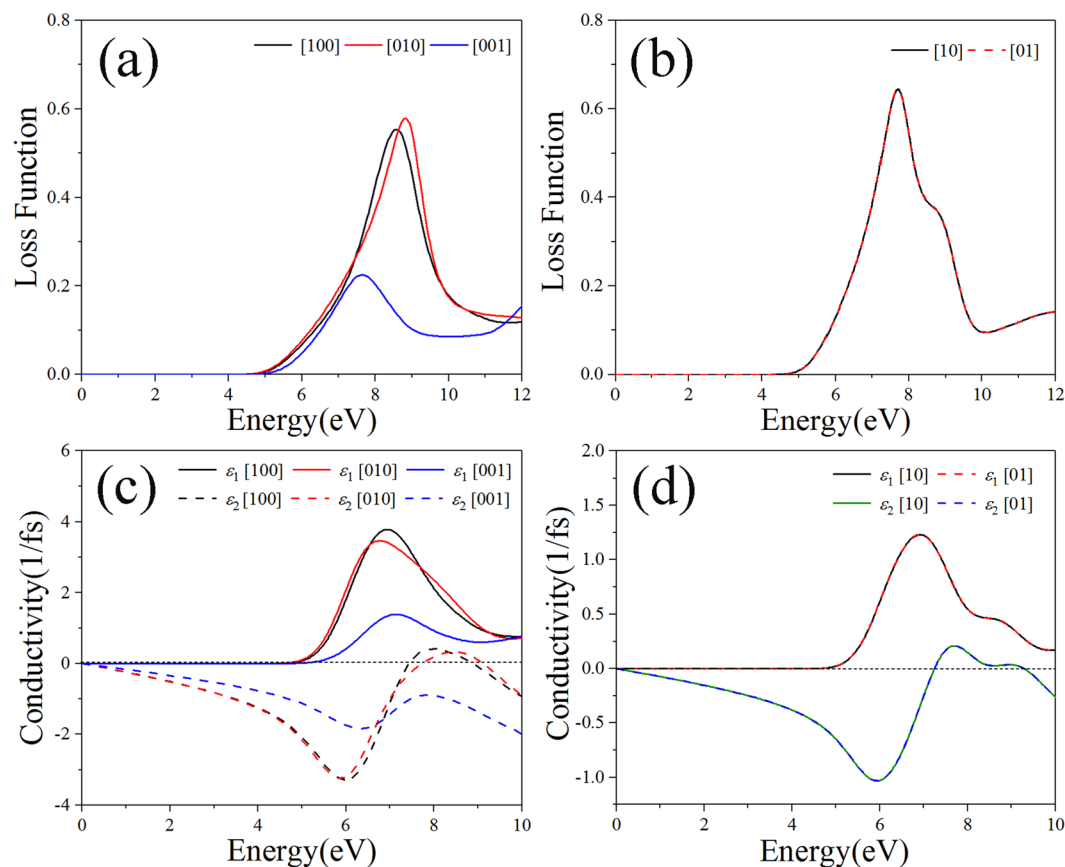


Figure 7. The loss functions and conductivities of **(a,c)** bulk B_4N_4 and **(b,d)** monolayer B_4N_4 .

2.36, and there are three major peaks locating at 5.88, 5.76 and 6.18 eV in $\varepsilon_1^{[100]}(\omega)$, $\varepsilon_1^{[010]}(\omega)$ and $\varepsilon_1^{[001]}(\omega)$, respectively. In $\varepsilon_2(\omega)$ of bulk B_4N_4 , there exist three major peaks locating at 6.84, 6.64 and 7.06 eV respectively corresponding to $\varepsilon_2^{[100]}(\omega)$, $\varepsilon_2^{[010]}(\omega)$ and $\varepsilon_2^{[001]}(\omega)$, which can be attributed to the electron transitions from N-2p to B-2p states. As regards to monolayer B_4N_4 in Fig. 5(b), however, the dielectric functions in [10] and [01] directions are completely the same, implying the influence of van der Waals force disappears. The theoretical static dielectric constants $\varepsilon_1^{[10]}(0)$ and $\varepsilon_1^{[01]}(0)$ are 1.59, and the same peak in $\varepsilon_1^{[10]}(\omega)$ and $\varepsilon_1^{[01]}(\omega)$ locates at 5.82 eV. $\varepsilon_2^{[10]}(\omega)$ and $\varepsilon_2^{[01]}(\omega)$ with their main peak sited at 6.79 eV originate from the electron transitions from N-2p to B-2p states.

The complex refractive index can be expressed as $\tilde{n}(\omega) = n(\omega) + ik(\omega)$, where the refractive index $n(\omega)$ has the same trend as the real part of dielectric function, while the extinction coefficient $k(\omega)$ is similar to the imaginary part of dielectric function. The refractive indexes and extinction coefficients of bulk B_4N_4 and monolayer B_4N_4 are respectively displayed in Fig. 6(a,b). The static refractive indexes $n(0)$ of bulk B_4N_4 are respectively 1.73, 1.74 and 1.54 along [100], [010] and [001] directions. For monolayer B_4N_4 , in [10] and [01] directions, the static refractive indexes $n(0)$ are 1.26. For bulk B_4N_4 , the maximum refractive indexes of [100], [010] and [001] directions are respectively 2.42, 2.42 and 1.87 at the photon energies of 5.91, 6.00 and 6.24 eV. For monolayer B_4N_4 , the energy-dependent refractive indexes in [10] and [01] directions reach the same maximum value of 1.58 at 5.91 eV. The extinction coefficients of bulk B_4N_4 and monolayer B_4N_4 are zero in the visible region. However, in the ultraviolet (UV) region, the extinction coefficients of bulk B_4N_4 have three peaks at 7.21, 7.06 and 7.18 eV respectively corresponding to [100], [010] and [001] directions, and those of monolayer B_4N_4 have the same peak at 7.07 eV in [10] and [01] directions.

The calculated absorption coefficients of bulk B_4N_4 and monolayer B_4N_4 are respectively shown in Fig. 6(c,d). The initial values of the first peak in the absorption spectra of bulk B_4N_4 and monolayer B_4N_4 are respectively 4.66 and 4.81 eV, which are significantly close to their band gaps. In the energy range of 0–10 eV, the absorption spectra of bulk B_4N_4 in [100], [010] and [001] directions respectively have their main peaks at 7.37, 7.43 and 7.28 eV, and those of monolayer B_4N_4 in [10] and [01] directions respectively have their main peaks at 7.17 eV. When the photon energy is greater than ~ 4.71 eV, bulk B_4N_4 and monolayer B_4N_4 begin to absorb incident light mainly in the ultraviolet region. In the considered energy region, bulk B_4N_4 has the highest absorption coefficient of $14.09 \times 10^4 \text{ cm}^{-1}$ at 7.37 eV in [100] direction. In the photon energy region of ~ 5 –9 eV, monolayer B_4N_4 can run up to the highest absorption coefficient of $6.59 \times 10^4 \text{ cm}^{-1}$. As a whole, the absorption coefficient of monolayer B_4N_4 is lower than that of bulk B_4N_4 in the energy region of 0–10 eV.

In the visible region, see Fig. 6(e,f), the reflectivities of bulk B_4N_4 in [100] and [010] directions ([001] direction) are about $\sim 7.7\%$ ($\sim 4.7\%$), and those of monolayer B_4N_4 in [10] and [01] directions are only $\sim 1.5\%$. In the

ultraviolet region, the highest reflectivity of bulk B_4N_4 is $\sim 22.29\%$ in [100] direction, while that of monolayer B_4N_4 is $\sim 7.30\%$. The reflectivity of monolayer B_4N_4 is much lower than that of bulk B_4N_4 . Consequently, monolayer B_4N_4 has a high transmissivity due to its low absorption and reflectivity, and it has potential applications in optoelectronic devices such as transparent electrodes.

Loss function depicts the energy loss of photoelectrons when they pass through uniform dielectrics, and the position of characteristic peak in loss function generally corresponds to the plasma frequency of dielectrics³⁴. The loss functions of bulk B_4N_4 and monolayer B_4N_4 are respectively plotted in Fig. 7(a,b), and one can see that the energy loss of photoelectrons occurs in the energy region greater than ~ 4.85 eV. The real and imaginary parts of the conductivities shown in Fig. 7(c,d) indicate that both bulk B_4N_4 and monolayer B_4N_4 have high conductivities in the energy range of ~ 6 – 8 eV and get their maximum conductivities at ~ 7 eV.

Conclusions

In the current work, we proposed bulk B_4N_4 and monolayer B_4N_4 and investigated their phonon dispersion relations, mechanical properties, electronic structures and optical properties by first-principles based on density functional theory. The crystal structure of bulk B_4N_4 consists of monolayer B_4N_4 connected by the van der Waals force, and the monolayer B_4N_4 is composed of four- and eight-membered rings. Bulk B_4N_4 and monolayer B_4N_4 are dynamically, thermally and mechanically stable. The elastic constants show that bulk B_4N_4 has large anisotropy. Moreover, through prediction of the PBE0 method, bulk B_4N_4 has an indirect band gap of 5.4 eV while monolayer B_4N_4 has a direct band gap of 6.1 eV. In either bulk B_4N_4 and monolayer B_4N_4 , the VBM is mainly contributed from B-2p and N-2p orbitals and the CBM mainly derives from B-2p states. Monolayer B_4N_4 with a high transmissivity has great potential in designing new optoelectronic devices such as transparent electrodes.

Received: 8 April 2019; Accepted: 16 December 2019;

Published online: 12 May 2020

References

- Pakdel, A., Zhi, C., Bando, Y. & Golberg, D. Low-dimensional boron nitride nanomaterials. *Mater. Today* **15**(6), 256–265 (2012).
- Pan, C., Zhang, J. Q., Kou, K. C., Zhang, Y. & Wu, G. L. Investigation of the through-plane thermal conductivity of polymer composites with in-plane oriented hexagonal boron nitride. *IJHMT* **120**, 1–8 (2018).
- Bourgeois, L., Bando, Y. & Sato, T. Tubes of rhombohedral boron nitride. *J Ph D* **33**(33), 1902 (2000).
- Tsao, J. Y. *et al.* Ultrawide-Bandgap Semiconductors: Research Opportunities and Challenges. *Adv Electron Mater.* **4**(1) (2018).
- Nagakubo, A., Ogi, H., Sumiya, H., Kusakabe, K. & Hirao, M. Elastic constants of cubic and wurtzite boron nitrides. *ApPhL* **102**(24), 055503 (2013).
- Mingsheng, X., Tao, L., Minmin, S. & Hongzheng, C. Graphene-like two-dimensional materials. *Chem. Rev.* **113**(5), 3766–3798 (2013).
- Ying, C., Jin, Z., Campbell, S. J. & Caer, G. L. Boron nitride nanotubes: Pronounced resistance to oxidation. *ApPhL* **84**(13), 2430–2432 (2004).
- Li, L. H. *et al.* Dielectric Screening in Atomically Thin Boron Nitride Nanosheets. *Nano Lett.* **15**(1), 218–223 (2015).
- Li, J., Li, H. & Yin, H. Structural evolution, tunable electronic and magnetic properties of bare and semi-hydrogenated two-dimensional cubic boron nitride nanosheets. *CPL* **610–611**, 198–203 (2014).
- Lin, S., Ye, X. & Huang, J. Can metal-free silicon-doped hexagonal boron nitride nanosheets and nanotubes exhibit activity toward CO oxidation. *PCCP* **17**(2), 888–895 (2015).
- Durandurdu, M. Hexagonal nanosheets in amorphous BN: A first principles study. *J. Non-Cryst. Solids* **427**, 41–45 (2015).
- Noorizadeh, S. & Shakerzadeh, E. Formaldehyde adsorption on pristine, Al-doped and mono-vacancy defected boron nitride nanosheets: A first principles study. *Comp Mater Sci.* **56**, 122–130 (2012).
- Lei, W. *et al.* Oxygen-doped boron nitride nanosheets with excellent performance in hydrogen storage. *Nano Energy* **6**, 219–224 (2014).
- Sch, K. D., Ouml, J. C. & Jansen, M. Structure prediction based on ab initio simulated annealing for boron nitride. *Phys. Rev. B* **78**(14), 012014 (2008).
- Li, X. D. & Cheng, X. L. Predicting the structural and electronic properties of two-dimensional single layer boron nitride sheets. *CPL* **694**, 102–106 (2018).
- Clark, S. J. *et al.* First principles methods using CASTEP. *ZKri* **220**(5/6/2005), 567–570 (2005).
- Perdew, J. P., Burke, K. & Ernzerhof, M. Generalized Gradient Approximation Made Simple. *Phys. Rev. Lett.* **77**(18), 3865–3868 (1996).
- Lavrentyev, A. A. *et al.* Electronic structure and optical properties of noncentrosymmetric LiGaSe₂: Experimental measurements and DFT band structure calculations. *Opt. Mater.* **66**, 149–159 (2017).
- Cohen, A. J., Mori-Sánchez, P. & Yang, W. Fractional charge perspective on the band gap in density-functional theory. *Ph Rv B* **77**(11), 115123 (2008).
- Fletcher, R. A new approach to variable metric algorithms. *Computer J.* **13**(3), 317–322 (1970).
- Born, M. & Huang, K. Dynamical Theory of Crystal Lattices. *Am. J. Phys.* **23**(2), 113–127 (2005).
- W. Voigt, Lehrbuch der Kristallphysik, Teubner Leipzig. 1928).
- A. Reuss, Berechnung der Fließgrenze von Mischkristallen auf Grund der Plastizitätsbedingung für Einkristalle, Z.ang.math.mech. 91929).
- Hill, R. The Elastic Behaviour of a Crystalline Aggregate, Proceedings of the Physical Society. Section A. **65**(5), 349 (1952).
- Ranganathan, S. I. & Ostoja-Starzewski, M. Universal elastic anisotropy index. *Phys. Rev. Lett.* **101**(5), 055504 (2008).
- Puigdollers, A. R., Alonso, G. & Gamallo, P. First-principles study of structural, elastic and electronic properties of α -, β - and γ -graphyne. *Carbon* **96**, 879–887 (2016).
- Zunger, A., Katzir, A. & Halperin, A. Optical properties of hexagonal boron nitride. *Phys. Rev. B* **13**(12), 5560–5573 (1976).
- Nikiforov, I. Y., Ilyasov, V. V. & Safontseva, N. Y. Electronic energy structure of non-stoichiometric cubic boron nitride. *Journal of Physics Condensed Matter* **7**(30), 6035 (1995).
- Solozhenko, V. L., Lazarenko, A. G., Petitet, J. P. & Kanaev, A. V. Bandgap energy of graphite-like hexagonal boron nitride. *J. Phys. Chem. Solids* **62**(7), 1331–1334 (2001).
- Töll, J. S. Causality and the Dispersion Relation: Logical Foundations. *Phys. Rev.* **104**(6), 1760–1770 (1956).
- Saha, S., Sinha, T. P. & Mookerjee, A. Electronic structure, chemical bonding, and optical properties of paraelectric BaTiO₃. *Ph Rv B* **62**(13) (2000).

32. Tripathy, S. K. & Kumar, V. Electronic, elastic and optical properties of ZnGeP₂ semiconductor under hydrostatic pressures. *Mater Sci Eng B-Adv.* **182**, 52–58 (2014).
33. Xiao, J., He, Z., Zhu, S., Chen, B. & Jiang, G. Hybrid functional study of structural, electronic, bonding and optical properties of CdSiP₂. *COMP. Mater Sci.* **117**, 472–477 (2016).
34. Duan, Y. H. & Yong, S. First-principles calculations of optical properties of Mg₂Pb. *Sci China.* **57**(2), 233–238 (2014).

Acknowledgements

The current work was supported by the National Natural Science Foundations of China (Grant No. 51171156, 51601153) and Chongqing Science & Technology Commission (Grant No. cstc2018jcyjx0582, cstc2017jcyjAX0195).

Author contributions

Nanpu Cheng put forward the original idea for this manuscript. Huayue Mei, Yuhan Zhong and Dafang He set up the models and proposed the calculation scheme. Huayue Mei, Xue Du, Chunmei Li, and Nanpu Cheng analyzed and discussed the calculation results. Finally, Huayue Mei organized and wrote this manuscript.

Competing interests

The authors declare no competing interests.

Additional information

Correspondence and requests for materials should be addressed to N.C.

Reprints and permissions information is available at www.nature.com/reprints.

Publisher's note Springer Nature remains neutral with regard to jurisdictional claims in published maps and institutional affiliations.



Open Access This article is licensed under a Creative Commons Attribution 4.0 International License, which permits use, sharing, adaptation, distribution and reproduction in any medium or format, as long as you give appropriate credit to the original author(s) and the source, provide a link to the Creative Commons license, and indicate if changes were made. The images or other third party material in this article are included in the article's Creative Commons license, unless indicated otherwise in a credit line to the material. If material is not included in the article's Creative Commons license and your intended use is not permitted by statutory regulation or exceeds the permitted use, you will need to obtain permission directly from the copyright holder. To view a copy of this license, visit <http://creativecommons.org/licenses/by/4.0/>.

© The Author(s) 2020